Ma, W., Macdonald, J. H. G., Liu, Q., Nguyen, C. H., & Liu, X. (2017). Galloping of an elliptical cylinder at the critical Reynolds number and its quasi-steady prediction. *Journal of Wind Engineering and Industrial Aerodynamics*, *168*, 110-122. https://doi.org/10.1016/j.jweia.2017.04.022

Galloping of an elliptical cylinder at critical Reynolds number and its quasi-steady prediction

Wenyong Ma[a,b], John.H.G. Macdonald[c], Qingkuai Liu[a,b], Cung. H. Nguyen[d], Xiaobing Liu[a,b]

[a]Wind Engineering Research Center, Shijiazhuang Tiedao University, Hebei 050043, China

[b]The Key Laboratory for Health Monitoring and Control of Large Structures, Hebei province, 050043, China

[c]Department of Civil Engineering, University of Bristol, BS8 ITR, UK

[d]Department of Civil Engineering, Industrial University of Ho Chi Minh City, Ho Chi Minh City 70000, Vietnam

Abstract: Dry galloping of inclined cables has been shown to have a strong relation to the critical Reynolds number. This study concerns the occurrence of galloping of an elliptical cylinder at critical Reynolds numbers under normal wind and an assessment of the quasi-steady assumption on predicting these vibrations. A series of static and dynamic wind tunnel tests are carried out to measure the wind pressure on a static cylinder and displacement of a three-degree-freedom vibrating cylinder. The static aerodynamic force on the cylinder shows the occurrence of reattachment which lowers the drag coefficient and increases the lift coefficient at critical Reynolds numbers. This phenomenon gives the possibility of satisfying the across-wind galloping criterion by adversely changing the aerodynamic force with the angle of attack. Meanwhile, unsteady and steady amplitude galloping are observed in dynamic tests in a certain range of Reynolds number and angle of attack. The observations indicate that the galloping is across-wind dominated and strongly depends on the Reynolds number. Finally, quasi-steady predictions of galloping instability are compared with the observed galloping. Most of the observed occurrences of galloping are in the predicted unstable range, but several other cases for which galloping was predicted do not exhibit large vibrations. This implies that the quasi-steady assumption does not work well in predicting the galloping of elliptical cylinders at critical Reynolds numbers.

Keywords: Wind tunnel test; Elliptical cylinder; Critical Reynolds number; Quasi-steady assumption; Galloping

1. Introduction

A large vibration of an inclined cable so-called dry galloping, which attracts much interest, has been addressed through a lot of experimental and theoretical studies because of its complicated aerodynamics (Cheng et al, 2008; Jakobsen et al, 2012; Macdonald and Larose, 2006, 2008a, b; Matsumoto et al, 2010; Nikitas and Macdonald, 2015; Raeesi et al, 2013). Thesevibrations occur for dry inclined cables without ice accretion and differ from both conventional across-wind galloping and wind-rain-induced vibrations. Actually, three branches have developed since 2003 that may possibly explain this phenomenon. The first believes the dry galloping is conventional across-wind galloping of an imperfect circular cylinder (Benidir et al, 2015; Matteoni and Georgakis, 2015) which satisfies the Den Hartog galloping criterion. The second explanation claims dry galloping might be highly related to mitigation of Karman vortex shedding, as is suggested also occurs for wind-rain-induced vibrations (Matsumoto et al, 2003; Matsumoto et al, 2010). The third suggests that dry galloping is related to some kind of organization of the noise that arises from the critical Reynolds number transitional behavior and possibly the ambient turbulence (Nikitas and Macdonald, 2015; Nikitas et al, 2012). Although the mechanism of dry galloping is still unclear, most researchers agree that the large amplitude vibrations are related to the critical Reynolds number, which has been shown significantly influences the flow patterns, aerodynamic forces and galloping instabilities for cylinders with smooth cross-sections, such as circular cylinder (Zdravkovich, 1997).

In the critical Reynolds number range, the boundary layer undergoes a flow transition and separation bubbles may form on one or both sides of the cylinder because of reattachment. Vortex shedding may also disappear(Ma et al, 2015; Zdravkovich, 1997). Furthermore, the flow in the critical Reynolds number range is sensitive to any disturbance including either cylinder motion or ambient flow conditions (Cao and Tamura, 2008; Rodríguez et al, 2013; Schewe, 1986). This sensitivity poses more uncertain factors on dry galloping response and its excitation mechanism. In order to get a better understanding of the effect of the critical Reynolds number on galloping response, the aeroelastic loading on a dry cable has been analyzed based on dynamic wind pressure tests in a wind tunnel. The results reveal an inherent

flow pattern unsteadiness in the critical Reynolds number range and its interaction with the moving cylinder(Nikitas and Macdonald, 2015; Nikitas et al, 2012), but more dynamic pressure tests are needed to make clear conclusions.

Most dry galloping has been observed in wind tunnel tests on inclined cables in critical Reynolds number range. Observations include the effects of Reynolds number, an axial flow which may mitigate Karman vortex shedding and uncertainty of imperfections which may give aerodyanmic coefficients satisfying the Den Hartog criterion. Since across-wind galloping was firstly proposed in 1932 by Den Hartog (DenHartog, 1932), it has been used to predict galloping instability and has been developed and allplied in many studies (Ng et al, 2005; Nikitas and Macdonald, 2014; Pa¨ıdoussis et al, 2011). It worked well for Reynolds number related galloping of an electiciy conductors at reduced velocity over 1000 (Macdonald et al, 2008) and fave reasonable agreement with evaluated aerodyanmic damping from full scale measument on twin cable bridge stays(Acampora et al, 2014). However, this criterion neglects the effect of the varing motion of structure on fluid around it and treats galloping as a quasi-steady process. For a perfect circular cylinder, there shoud be no Den Hartog galloping because the crierion assumes that the change of aerodynamic force depends on the changing relative angle of attack. However, in wind tunnel tests on circular cylinders, it has been proved that surface roughness and circularity defects can have a significant effect on both mean aerodynamic forces and galloping instability. Benidir et at (Benidir et al, 2015) find that the roughness and circularity defects cause earlier or later appearance of boundary layer transitions and the occurrence of jumps in the instantaneous lift between two or more quasi-stable states. Matteoni and Georgakis (Matteoni and Georgakis, 2015) point out that dry cable instability is very sensitive to microscopic geometrical imperfections of the cable model, which can trigger the vibrations in the critical Reynolds number range with either positive or negative aerodynamic damping. These findings imply that geometrical imperfections or surface roughness may induce large vibrations in the critical Reynolds number range, but the mechanism is not as simple as the Den Hartog criterion.

The sensitivity of the aerodynamic forces on circular cylinders to surface conditions in the critical Reynolds number range make it a challenge to use the quasi-steady assumption for predicting galloping instability. Meanwhile the existence of axial flow on inclined cables make it even harder to the identify effects of Reynolds number. To reduce the problem to a more clear and simple case, an elliptical cylinder is tested under normal wind to address the critical Reynolds number effect. The ellipse has similar aerodynamic characteristics to a circular cylinder, but it has a clear defined angle of attack, rather than the sysmetry just being small geometrical imperfection or surface roughness. Also the axial flow is likely to be negligible under normal wind. Assessing the possibility of galloping of an elliptical cylinder in the critical Reynolds number range and the ability of the quasi-steady assumption to predict the vibrations will give better understanding of galloping at critical Reynolds number.

In this study, an elliptical cylinder with a ratio of major to minor axis of 1.5 is tested in a wind tunnel to determine the pressure distribution and its galloping response. The aerodynamic forces are measured by using 320 pressure taps on four cross-sectional rings and four lines along the length of cylinder. The characteristics of the aerodynamic forces on the cylinder in the critical Reynolds number range are described. Based on the quasi-steady assumption, static aerodynamic forces are used to predict galloping instability. Meanwhile, galloping is observed in dynamic tests. By comparing the observed galloping with the predicted galloping, the validity of the quasi-steady assumption on predicting galloping at critical Reynolds number is discussed.

2. Experimental setup

Tests were carried out at Shijiazhuang Tiedao University in the STDU-1 wind tunnel; a closed-circuit wind tunnel having a larger test section 4.38 m wide, 3 m high and 24 m long; and a smaller one 2.2 m wide, 2 m high and 5 m long. The model and supporting system were in the larger test section in which the velocity profile was uniform within ±0.5% and the turbulence intensity was approximately 0.5% at 20m/s. The aerodynamic coefficients were calculated from the integral of the pressure coefficients over the perimeter of the cross-section. C_P, C_D, C_L, C_M and are defined as the mean pressure coefficient, drag coefficient, lift coefficient and moment coefficient, while $C_{P\sigma}$ is the standard

deviation of the pressure coefficient. The Reynolds number *Re* is defined as $Re=\rho DU/\mu$, where ρ, U and μ are the air density, mean oncoming wind velocity and dynamic viscosity of the air, respectively.

The elliptical cylinder model had a length L of 2900 mm, a minor axis D of 180 mm, and a major axis of 1.5D. The model was made of polyethylene pipe. Since the model and supporting system were in the wind tunnel, the end conditions may have a significant influence on the wind pressure distribution. Unfortunately, it is hard to eliminate this effect completely. A fixed end plate is a commonly used way to reduce this impact, but it prevents the possible axial flow for a skew cylinder (Yagi et al, 2009)(which it is planned to test in the next stage of our studies) and induces an additional aerodynamic force when it vibrates in dynamic tests. A compensation model on both ends also is a choice to lessen the end effects, but it cannot be used in dynamic tests as well because the compensation part will not have vibrations the same as the cylinder model. In order to keep the same end conditions for both static and dynamic tests for both normal and skew cylinder, a fixed end plate with a hole in the center and an end cover are used at each end. Each end plate has a length of 2280mm and a circular hole with a diameter 300 mm at its center. An end cover with a shape of NACA2420 was connected to the endplate to reduce the effects of flow around the cylinder end and the supporting system on the aerodynamic forces and vibrations Fig. 1 (a). In this arrangement, the supporting system and cylinder ends were enclosed by the end plates and covers, and cylinder could move in the holes on the center of the end plates. An end bar was used at each end to fix the model for the static tests or hang springs for the dynamic tests.

Pressure measuring taps were arranged at four discrete cross-sections (termed Rings A, B, C and D) and four axial lines (termed L1, L2, L3 and L4). Ring C is in the middle of the cylinder, Ring B is 20cm from Ring C, while Rings A and D are 85cm from the ends of the cylinder Fig. 1 (b). The four axial lines are located at both ends of the major and minor axes of the cross-section. Each ring has 50 taps around the circumference and each line has 30 taps uniformly distributed along the cylinder axis at spacings of 94mm, 87mm at each end. The pressure tubes were all in length 800mm and their effect on pressure distortion was corrected by using the frequency-response function of each tube. The aerodynamic pressure was collected with pressure sensors (ESP-64Hd, Measurement Specialties (formerly PSI), Hampton, VA, USA) and a data acquisition system (DTC Initium, Measurement Specialties) with record lengths of 80 s with a sampling frequency of 331.60 Hz.

2.1 Static tests

Static pressure tests were carried out to obtain the static aerodynamic forces on the cylinder.The wind speeds were 5m/s and from 10m/s to 20m/s in 2m/s intervals, which corresponds to Reynolds number from approximately 0.61×10^5 to 2.45×10^5 (based on the minor axis D) for the static tests. The angles of attack α were from wind parallel to the major axis, 0°, to parallel to the minor axis, 90°, at 10° intervals in general and at 2° spacing in the range 20°-30°.

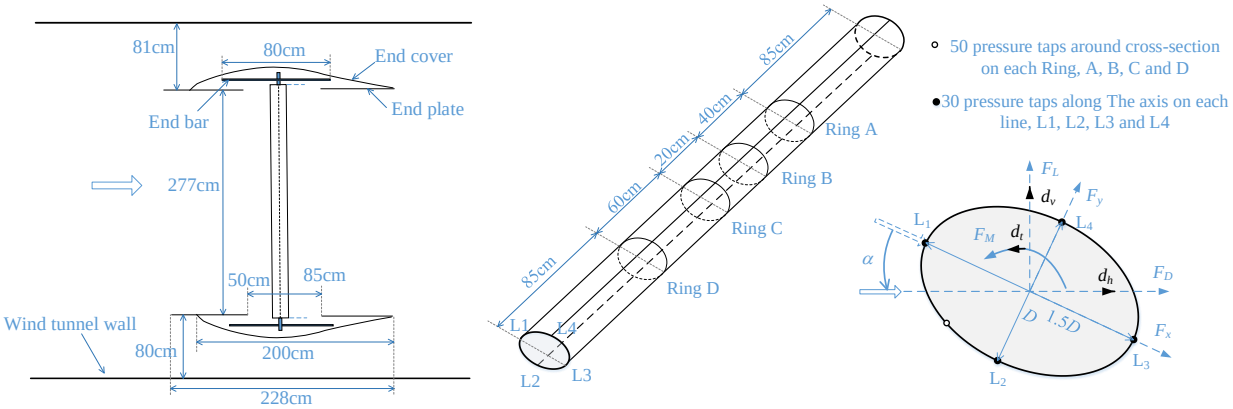

(a) Model arrangement (b) Pressure tap arrangement and parameter definition

Fig. 1. Schematics of wind tunnel arrangement and the model with the main parameters indicated.

2.2Dynamic tests

Dynamic tests were carried out with the same model arrangement as in the static tests, except the model was supported by a system that allowed vibration in three-degrees-of-freedom. The support system comprised four inclined springs and an end bar at each end as shown in Fig. 2. The natural frequencies in the vertical, horizontal and torsional degrees of freedom f_V, f_H and f_T, respectily are functions of the mass m, rotational inertia m_T and spring. The displacements were measured with laser displacement sensors (Panasonic HL-G112-A-C5) at both ends for the vertical and torsional motions and a sensor at one end for horizontal motion. Free vibration tests were carried out to obtain the decay of vibraions in the vertical d_v, horizontal d_h and torsional d_t. The natural frequencies and damping ratios were identified through the Fast-Fourier-Transform and logarithmic decrement of displacement. Structural dynamic parameters are shown in Fig. 2 as well. The identified natural frequencies of 2.03Hz vertical, 1.64Hz horizontal and 7.14 Hz torsional agree well with the calculated values 2.07Hz in vertical, 1.60Hz in horizontal and 7.31 Hz in torsional.

For the dynamic tests, the aerodynamic forces from static tests were used to estimate the mean torsional displacement of the cylinder to aim to achieve specific angles of attack at certain Reynolds number. The cylinder was mounted at an initial angle of attack α_0 for no wind. Then the wind speed increased to a certain value and kept steady for at least 6 minutes to observe possible vibrations and record the displacements and wind pressures at this wind speed. The mean angle of attack α was larger than α_0 due to the wind-induced torsion. The wind speed in the dynamic tests was from 0 to about 18m/s at minimum intervals of 0.1m/s in the critical Reynolds number range in many cases. Five initial angles of attack α_0=23.20°, 24.50°, 25.50°, 26.00° and 28.00° were tested, and the range of angles of attack under wind speeds up to 18m/s was from 23.20° to 30.60°. Most of the angles of attack in the dynamic tests were intentionally designed to be in the unstable range predicted from static aerodynamic forces though the quasi-steady assumption. In order to verify the observed vibrations, the same process was carried out twice. Sometimes the development of steady-state vibrations takes time, so the sampling period is a parameter difficult to choose in the dynamic tests. For the cases in this study the vibrations were observed in at least two minutes before and around two minutes after recording, except for the records aiming to catch a diverging or diminishing process. For the dynamic tests, the record length was still 80 s, buth the sampling frequency for the displacments was 500Hz.

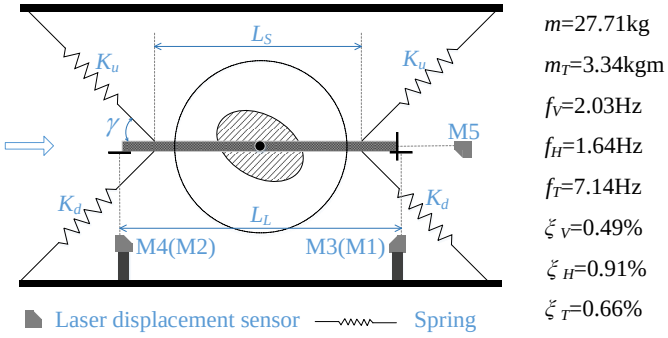

Fig. 2. Schematic of the support system at each end of the model, along with its dynamic parameters.

3. Static experimental results

3.1Wind pressure distribution on circumference

The mean and standard deviation of pressure coefficient on four rings at Re=1.47×10^5, 1.96×10^5 and 2.22×10^5 are shown in Fig. 3 in which the thick solid line, the dashed line and the circle symbol represent the shape of the cross-section, mean pressure coefficient distribution and the maximum of the mean pressure coefficients, respectively. The filled area in Fig. 3 is from the mean value minus the standard deviation to plus the standard deviation to indicate a

strength of the pressure fluctuations. At Re=1.47×10^5 in Fig. 3, the wind pressure distributions on the four rings are very similar, then, when Reynolds number is up to 1.96×10^5, the distribution changes obviously on Ring B and stays similar to that at Re=1.47×10^5 on Rings A and C. The distributions on Rings C and D at Re=2.22×10^5, which differ from that at Re=1.47×10^5 and 1.96×10^5, become similar to that on Ring B. These changes of pressure distribution at various Reynolds numbers can be explained by the widely accepted reason of the formation of a separation bubble due to flow reattachment occurring in the critical Reynolds number range (Zdravkovich, 1997) . The flow reattaches on Ring B at Re=1.96×10^5 and on Rings B, C and D at Re=2.22×10^5. Interestingly, it seems that the flow around Ring A at Re=2.22×10^5 is experiencing a transition from the subcritical to the critical, giving strong pressure fluctuations which will be discussed later. Furthermore, the results shown in Fig. 3 reveal that the flow around Ring B reattaches at a lower Reynolds number than that on the other rings and implie that the flow around the cylinder is not two-dimensional for some reason relating to the three-dimensional characteristics of flow, an imperfection of the surface of the cylinder, non-uniformity of the approaching flow or some other reson. This three-dimensional behavior in critical Reynolds number range has been reported previously for circular cylinders (Benidir et al, 2015; Jakobsen et al, 2012). It was attributed to imperfections of the surface or slight lack of circularity of the cylinders giving local asysmetry. However, even for the elliptical cylinder, with its clear regular lace of circularity the pressure distribution is not uniform over the length in the critical Reynolds number range. The pressure distributions on the four rings also show differences in the location of final separation point, which at Re=2.22×10^5 is more leeward on Ring B than on Rings C and D. This non-uniformity of pressure along the cylinder axis poses a technical challenge in estimating the total aerodynamic force on the cylinder. Fortunately, there are many clear characteristics of wind pressure in the critical Reynolds number range. These characteristics and the wind pressure distribution along the length will be discussed and used to estimate the mean wind pressure distribution on unmeasured cross-section in the next section.

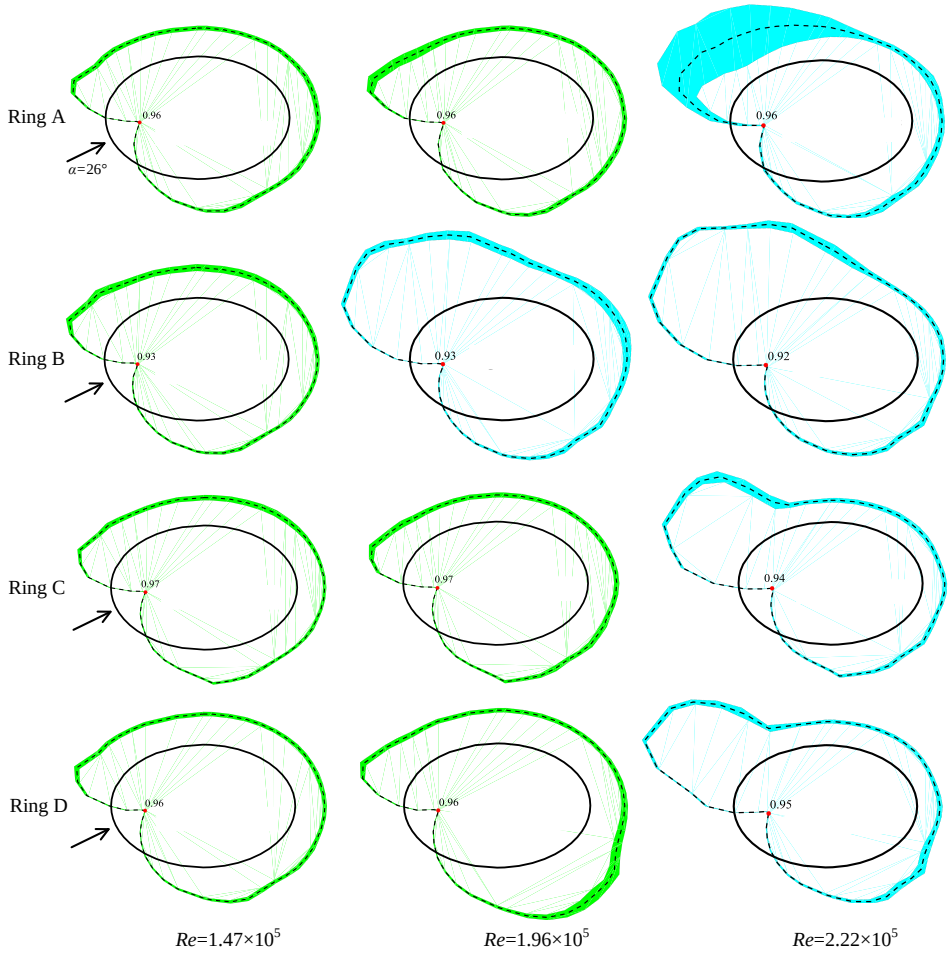

Fig. 3 The mean and standard deviation of pressure coefficient distribution on four rings at α=26°, Re=1.47×10^5, 1.96×10^5, and 2.22×10^5

Fig. 4 shows the variation of the mean (C_D, C_L and C_M) and standard deviation ($C_{D\sigma}$, $C_{L\sigma}$ and $C_{M\sigma}$) aerodynamic coefficients on the four rings with Reynolds number at α=26°. At lower Reynolds numbers, both mean and standard deviation values exhibit good agreement along the length. This agreement is broken with the reduction of mean drag coefficients and increase of mean lift coefficients, which are a clear sign of the occurrence of flow reattachment at critical Reynolds numbers. During the drag reduction processes, corresponding to the well-known drag crisis phenomenon on circular cylinders, the difference between the mean aerodynamic coefficients on the four rings is significant. The process starts at lower Reynolds numbers on some rings than on others. It appears they stop at different Reynolds numbers as well. The fluctuation of the aerodynamic force coefficients is strong for Ring A at Re=2.22×10^5 (in Fig. 4) because of the strong pressure fluctuation in the separation bubble area (shown in Fig. 3).

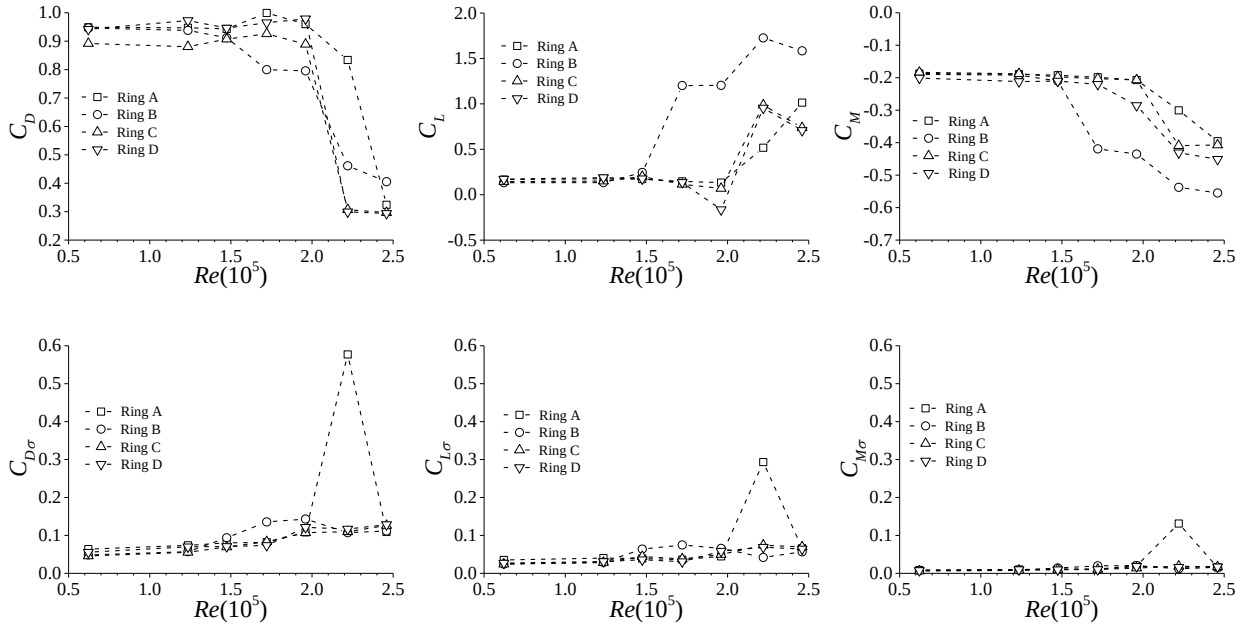

Fig. 4 Variation of the mean and standard deviation of aerodynamic coefficients on the four rings with Reynolds number, at α=26°.

Time histories of the aerodynamic coefficients C_D(t), C_L(t)and C_M(t) for Ring A at Re=2.22×10^5 and α=26°are shown in Fig. 5. The results at Re=2.45×10^5 are also shown to indicate the super-critical behavior.

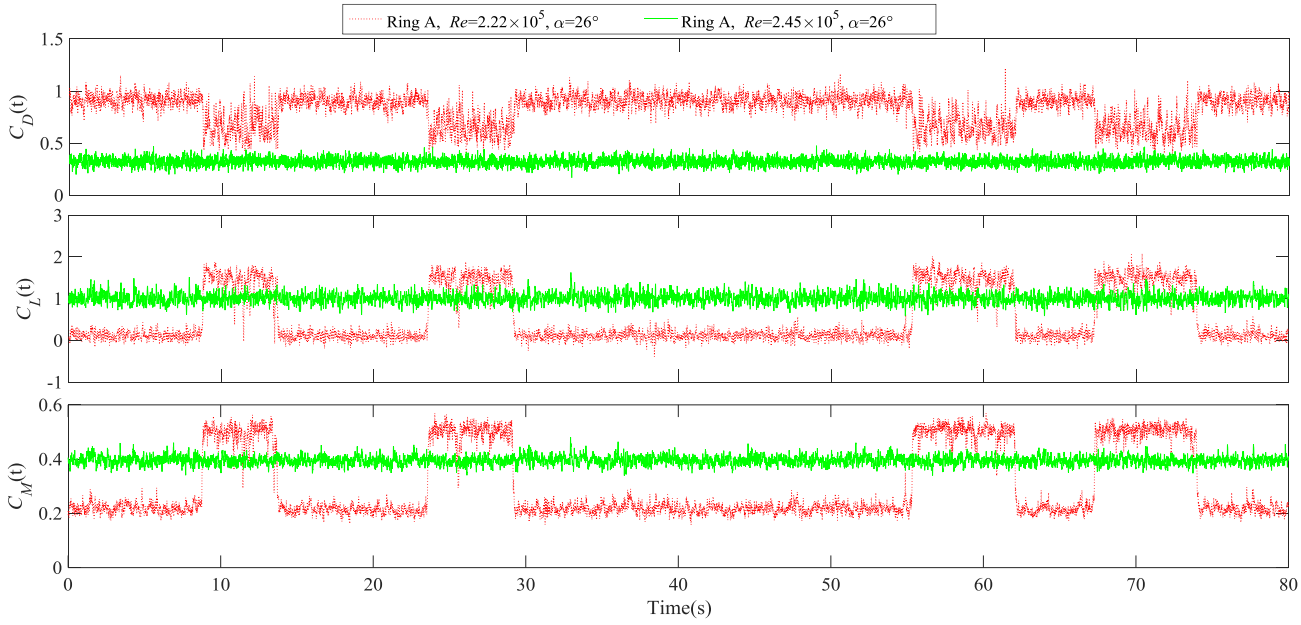

Fig. 5 Time histories of aerodynamic force coefficients on Ring A at α=26°, Re=2.22×10^5 and 2.45×10^5.

The aerodynamic coefficients at Re=2.22×10^5 undergo a series of jumps which imply an unstable transition from the subcritical Reynolds number state to another state at the critical Reynolds numbers. Taking the instantaneous lift coefficients as an example, it jumps between around 0.15 and 1.50 at Re=2.22×10^5 and stays at 1.0 at Re=2.45×10^5. This phenomenon has been studied on circular cylinders recently and it may have a significant role in inducing large vibrations (Matteoni and Georgakis, 2015; Nikitas and Macdonald, 2015). These jumps show that reattachment is not a gradually developing process. A large lift coefficient appears once the flow reattaches. The values in the transition state do not represent the values in the states before and after the transition. The lift coefficient at 2.45×10^5 is between the jumping values.

3.2 Wind pressure distribution along the length

The pressure distribution on an infinite length cylinder might be supposed to be uniform along the axis of the cylinder under a stable uniform flow, but it is much more complicated for a finite length cylinder in wind tunnel tests, especially in the critical Reynolds number range because of disturbance of flow condition, model uniformity, and end effects. As we will predict galloping instability of the cylinder based on the quasi-steady assumption which mainly depends on the total aerodynamic force acting on the cylinder, the pressure distribution along the length can provide an accurate estimation of the total force other than using pressure on a few cross-sections.

The mean and standard deviation of the pressure coefficient distribution along the axis of the cylinder at the angle of attack α=0° at different Reynolds numbers are shown in Fig. 6. The horizontal axes in Fig. 6 represent a ratio of a cross-section distance L_i to model length L. It indicates that approaching flow is uniform in both speed and turbulence intensity and implies an efficiency of end plates because the pressure on windward side line (L1) is uniform along the most length of the axis in all cases. Mean pressure distribution on the leeward side also has good uniformity. A big difference appears on both sides (L2 and L4) where flow experiences separation, reattachment, and transition in high Reynolds number range. Furthermore, the difference shows a sensitivity of flow in critical Reynolds number regime, as sharp pressure change occurs with a small Reynolds number variation from Re=1.72×10^5 to 1.96×10^5. The results shown in Fig. 6 also illustrate the end effects on wind pressure, and this may mainly be induced by the hole in end plate. However, this unwanted effects do not strongly affect the mean and standard deviation of pressure on four rings. End effects only influence the mean pressure up to around 10% of the length along the cylinder from each end. Based on these, even though the aerodynamic force is influenced by end conditions at a certain point, the significant difference of aerodynamic coefficients on four rings is induced by inherent characteristics of flow in specific Reynolds number range.

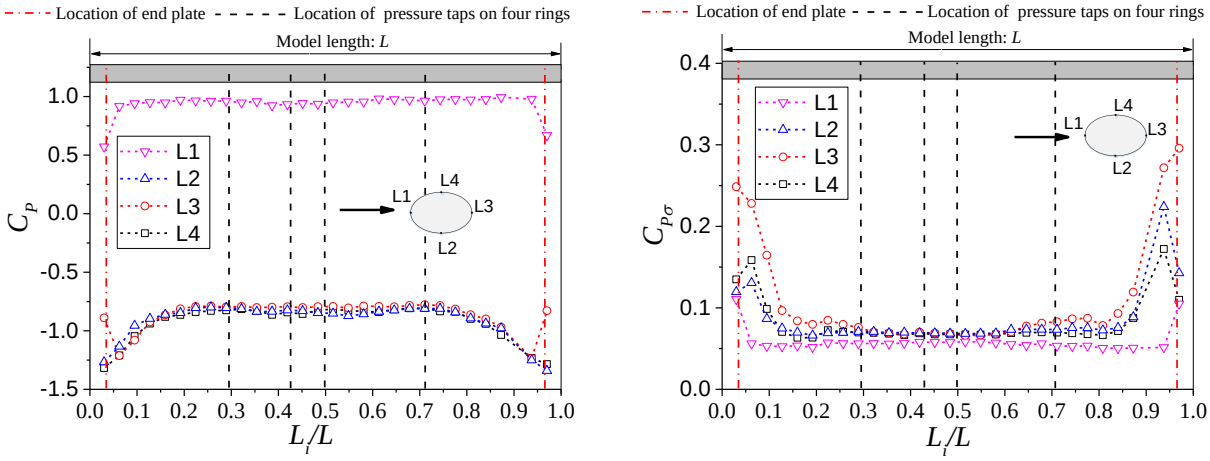

(a) Re=0.61×10^5

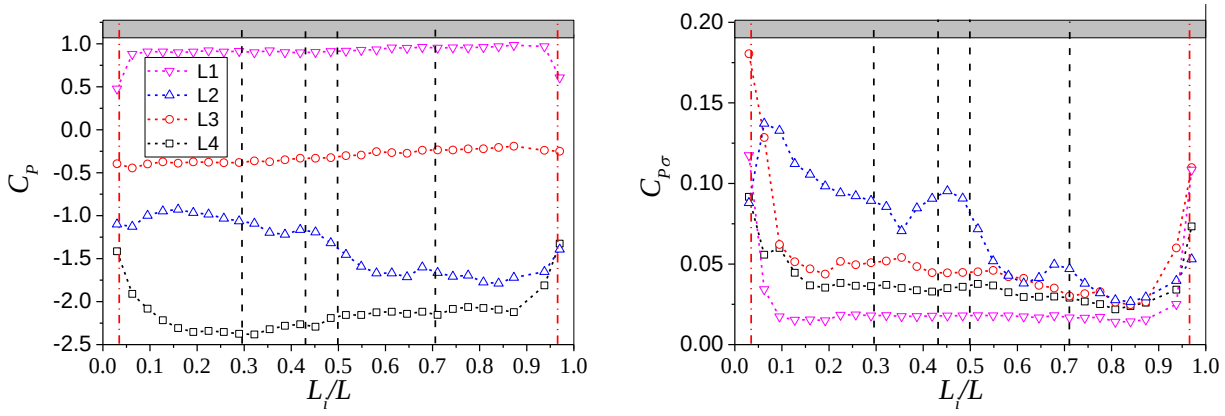

(b) Re=1.71×10^5

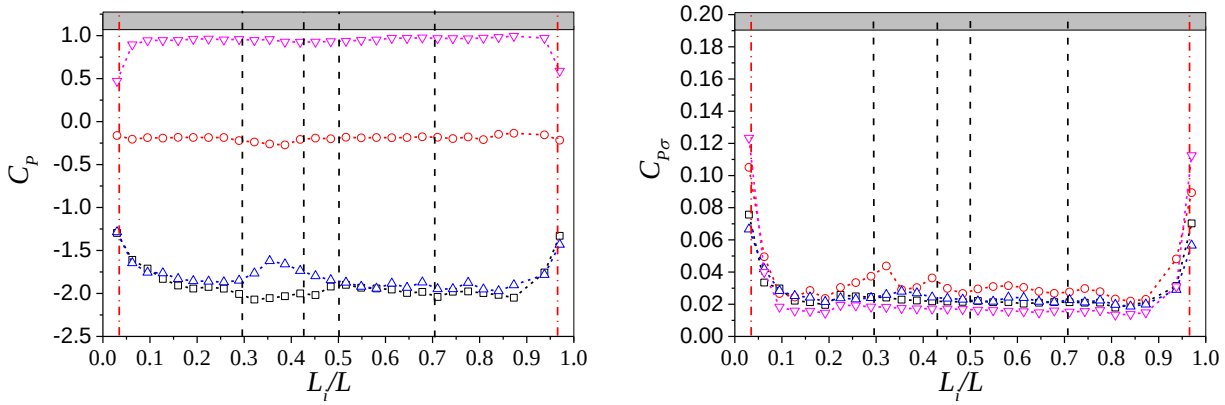

(c) Re=1.96×10^5

Fig. 6 The mean and standard deviation of pressure coefficients distribution on L1, L2, L3 and L4 in static tests at α=0° at Reynolds number of (a) Re=0.61×10^5, (b) Re=1.72×10^5, (c) Re=1.96×10^5

In order to estimate the total aerodynamic force on the cylinder, the wind pressure distribution on unmeasured cross-sections could be estimated by the pressures on L1, L2, L3 and L4. We assume that mean wind pressure distribution on every cross-section could be represented by the mean pressure value on the four measured rings (Ring A, B, C and D). Based on facts shown in Fig. 3 and Fig. 6 that the wind pressure on an individual cross-section may be very different with, three steps are included to estimate the mean wind pressure distribution on an unmeasured cross-section. The first step is to identify whether reattachment occurs on the estimating cross-section and choose the wind pressure distribution from four measure rings which have a similar reattachment state with the estimating cross-section. Then, the mean wind pressure on four line (L1 to L4) on the estimating cross-section are compared with their counterpart on the chosen rings by their difference calculated with least square method. Finally, a linear combination of the mean pressure on the chosen rings is used to represent the mean wind pressure on the estimating cross-section.

The most important step to estimate wind pressure distribution on an estimating cross-section is to recognize whether reattachment occurs because it has a significant influence on pressure as seen in Fig. 3. In identifying an occurrence of reattachment, the traits induced by reattachment are used. Although the traits are clear, the pressure on the four points (L1, L2, L3 and L4) may miss several of these traits due to the limitation of their locations. Generally, the clearest feature is a strong suction on where the separation bubble is formed. Furthermore, the pressure on reattachment side fluctuates severely sometimes, yet it may not clear enough to identify the reattachment. However, many profound

characteristics are also helpful on representing this phenomenon such as the disappearance of strong vortex shedding due to an interruption of wake flow communication by reattachment. Fig. 7 shows the mean, standard deviation and power spectral density of the pressure coefficients on L1, L2, L3 and L4 on Ring B at α=26° for the case with reattachment at Re=1.96×10^5 and the case without reattachment at Re=0.61×10^5. The wind pressure distributions corresponding to are shown in Fig. 3. Comparing with the non-reattachment state shown in Fig. 7 (a), when flow reattaches on the cylinder in Fig. 7 (b), the suction on L4 becomes strong changing from C_p=-0.85 to C_p=-1.4, and fluctuating becomes severe from $C_{P\sigma}$=0.09 to $C_{P\sigma}$=0.14, and the dominating frequency at fD/U=0.16 related to vortex shedding disappears. Another clear trait is also useful. When vortex shedding occurs, the fluctuating pressure around cylinder are influenced by it, and $C_{P\sigma}$ on L1 to L4 are similar. When flow reattaches on one side, the pressure on reattaching side fluctuates more severe that on that the other side. These severe fluctuating pressure in the critical Reynolds number range is mainly contributed by the lower frequency instead of by dominating vortex shedding frequency in the subcritical Reynolds number.

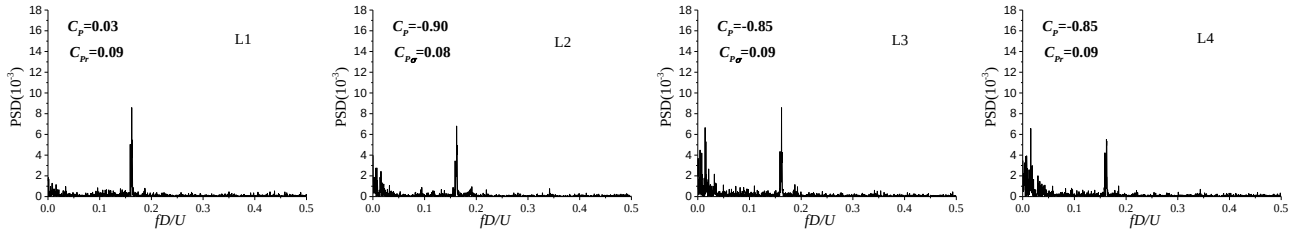

(a) Re=0.61×10^5

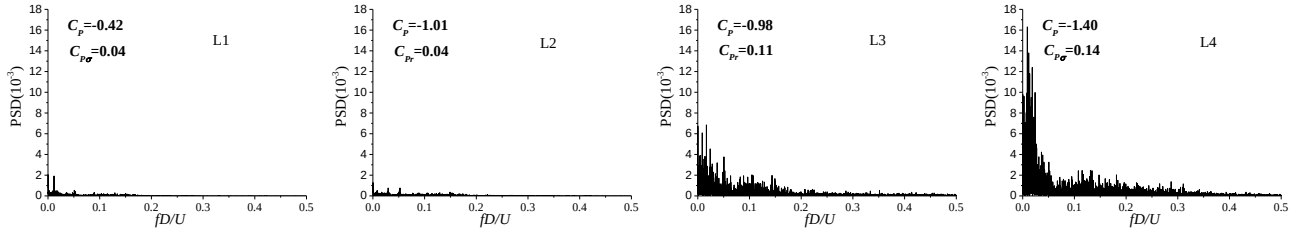

(b) Re=1.96×10^5

Fig. 7 The mean, standard deviation and power spectrum density of pressure coefficients on L1, L2, L3 and L4 on Ring B in static tests at α=26° at Reynolds number of (a) Re=0.61×10^5, (b) Re=1.96×10^5

The difference of wind pressure on an estimating cross-section $C_{Pj}^{\ i}$ and a chosen ring $C_{Pj}^{\ k}$ is calculated by the following equation.

$$Er_i^k = \sqrt{\sum_{j=L1}^{L4} \left(C_{Pj}^{\ i} - C_{Pj}^{\ k} \right)^2} \tag{1}$$

Where Er_i^k is the difference of mean pressure on the estimating cross-section i and the measure ring k; j is the symbol of pressure points on the circumference from L1 to L4; i is cross-section number from 1 to 30; and k is the symbol of chosen rings and comes from ring A, B, C or D.

For an individual cross-section, the aerodynamic coefficients on it can be calculated by a linear combination of the forces on the chosen rings. The weighting factor of each chosen ring k on estimating cross-section i Co_i^k is proportion to the 1/ Er_i^k.

$$Co_i^k = \left(1/Er_i^k\right) \Big/ \sum_k \left(1/Er_i^k\right) \tag{2}$$

Generally, the weighting factor for cross-section i can be calculated by this method if the similar rings are chosen. Unfortunately, the wind pressure distribution near the end of the cylinder (around 10% percent of the whole length) does not show similarity with the pressure on any of four measured rings. In this case, the relative similar one having the smallest Er_i^k will be chosen and the weighting factor of this ring will be 1.

Then, the aerodynamic force coefficients on an estimating cross-section are obtained by equation (4). The total aerodynamic coefficient which can represent the total force on the cylinder is an average of aerodynamic force coefficients on whole 30 cross-sections. This coefficient will be discussed in next section and used to estimate the galloping instabilities.

$$C_D{}^i = \sum Co_i^k C_D{}^k \qquad C_L{}^i = \sum Co_i^k C_L{}^k \qquad C_M{}^i = \sum Co_i^k C_M{}^k \tag{3}$$

The mean drag and lift coefficients along the length at α=26° are shown in Fig. 8 to illustrate variation of wind forces along the cylinder length. At Re=1.72×10^5 and 1.96×10^5, only two specific ranges of L_i/L from 0.32 to 0.48 and from 0.74 to 0.96 have large mean lift coefficient, which means reattachment only occurs at these two ranges. Rather than keeping uniform along the length at low Reynolds numbers, the strong varying distribution of aerodynamic force along the length at Re=2.22×10^5 and 2.45×10^5 means that reattachment may produce different strength separation bubbles in different cross-sections. It should be highlighted that the aerodynamic force distribution estimated by the proposed method is more accurate than an average of forces on four rings for it considers a more likely possible distribution, but we still can not identify how accurate it is because of lack of predictable techniques on characteristics of flow in critical Reynolds number and complex flow on the ends. As an example shown in Fig. 6, an obvious different wind pressure can be identified in the ends around 10% to 15% in total length, and its influence depends on Reynolds number as well.

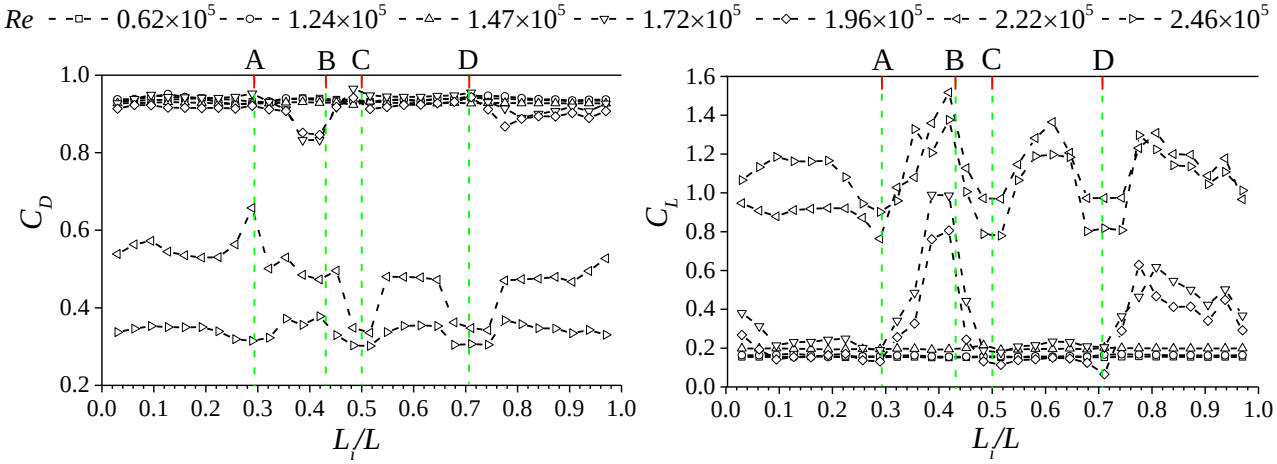

Fig. 8 The mean drag and lift coefficients on 30 cross sections along the length at α=26°

The mean displacement in dynamic tests can also be used to estimate the total aerodynamic coefficients on the cylinder, but it is not applied in this study for two reasons. On one hand, it is technically hard to control the angle of attack in the dynamic tests and only a few dynamic tests were carried out. It is not enough to predict the galloping instability. On the other hand, for the onset of galloping, according to quasi-steady theory, we need the forces in the static case. In the dynamic case, the mean forces may be different.

3.3Mean aerodynamic forces

The change of the wind pressure distribution induced by reattachment is obviously reflected in the mean aerodynamic forces shown in Fig. 9. The drag, lift and moment coefficients on the four measured rings are presented in Fig. 9 to show the difference of the aerodynamic coefficients along the cylinder. The average and weighted average aerodynamic coefficients are also shown in Fig. 9. The 'average' result is the mean aerodynamic coefficients on the four measured rings. In the weighted average method, weight factors Co_i^k is calculated by using equation (2), and weighted average force coefficients are calculated by equation (3). The results from both methods are close to each other in many cases, but they also show a large difference when the pressure distributes differently along the length. In fact, this difference mainly appears in the critical Reynolds number range in which the flow is more likely to be influenced by small

disturbance and shows the three-dimensional characteristics.

Comparing with the result of Re=0.61×10^5 (Fig. 9 (a)), the variations of mean aerodynamic coefficients with angle of attack from 0° to 30° are significantly affected by the critical flow state at Re=1.71×10^5 and from 0° to 50° at Re=2.22×10^5. Because the Reynolds numbers at which the reattachment occurs are different at each angle of attack, the flow reattaches at higher Reynolds number for the larger angle of attack in this study. A possible explanation is the smaller angle of attack has larger radius of curvature near the separation points which produces a relative high equivalent Reynolds number. When α=0° and Re=0.61×10^5, the lift coefficient is close to zero due to the symmetricity, and it is up to around 1 at Re=1.71×10^5 due to reattachment on one side, then it is back to around 0.15 at Re=2.22×10^5 because of an occurrence of reattachment on both sides. Taking the change of lift at α=0° into account, the lifts on the four rings are similar at Re=0.61×10^5 (in the subcritical range), then show the big difference at Re=1.71×10^5 (in the critical range) and are similar again at Re=2.22×10^5 (above the critical range). These imply the phenomenon which also can be found in Fig. 6 that the aerodynamic force distribution along the length may only show big difference at the critical Reynolds number. This also can explain the lift on four rings at α=35° showing the similarity at Re=1.71×10^5 and the big difference at Re=2.22×10^5.

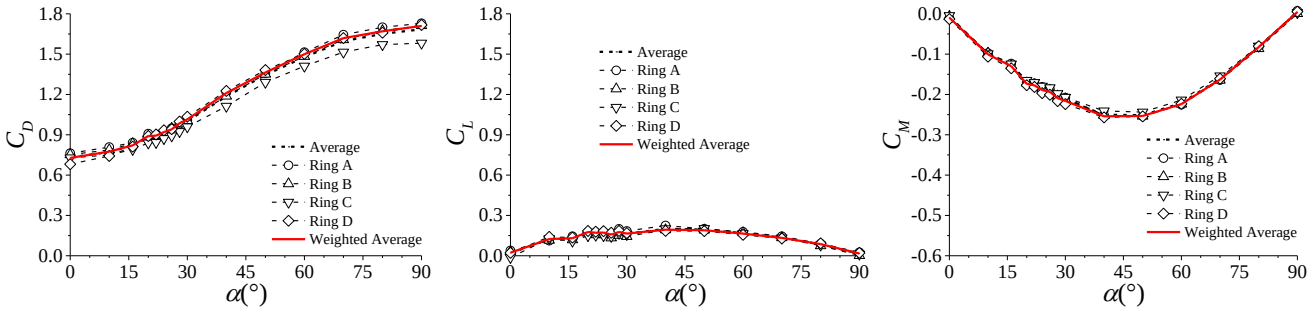

(a) Re=0.61×10^5

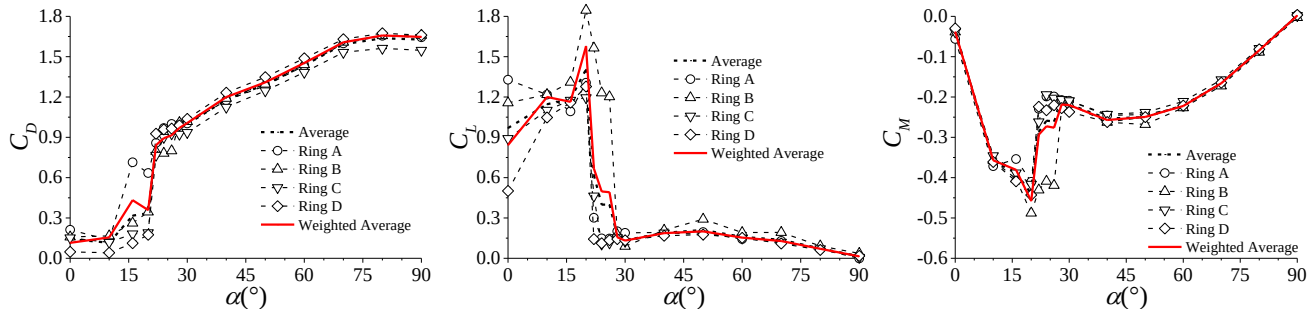

(b) Re=1.71×10^5

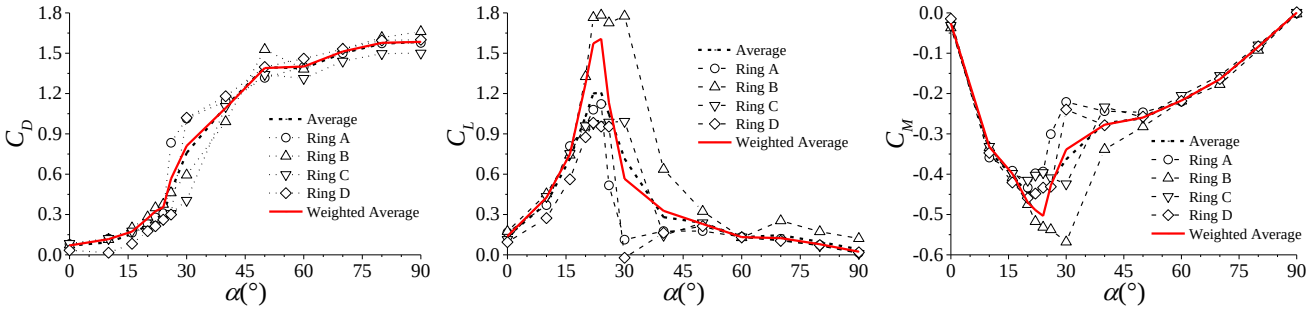

(c) Re=2.22×10^5

Fig. 9 Mean aerodynamic coefficients on the four rings at: (a) Re=0.61×10^5, (b) Re=1.71×10^5, (c) Re=2.22×10^5

Influences of the critical Reynolds number on the mean aerodynamic coefficients include lowering the drag coefficient, increasing the lift and moment coefficients, and most importantly, they create a sharp drop in the curves of lift coefficient against angle of attack which may satisfy the conventional cross-wind galloping criterion. More generally, the criterion assumes smooth changes in the aerodynamic coefficients with angle of attack. when there is reattachment,

this may not be the case. However, conventional cross-flow galloping theory explains its mechanism by using the similar curve of the lift coefficient against tangle of attack which may not associate with separation bubble. On the other hand, some researchers claim that reattachment is the generation mechanism of galloping because it interrupt the communication between upper and lower separated flows(Matsumoto et al, 2010). Taking into account the fact that the result shown at the angle of attack from 20° to 30° physically satisfies both explanations, the dynamic tests are carried out in this range and will be introduced in next section.

4. Dynamic experimental result

4.1 Occurrence of galloping

In the dynamic tests, many large vibrations were observed. Small increases in wind speed were in the region of the most severe vibrations to catch the processes of these large vibrations. At the initial angle of attack α_0=25.5°, the development of the large vibration is recorded and shown in Fig. 10, where dimensionless displacement is represented by displacement over diameter D in both vertical and horizontal axis. When the wind speed increases, the mean moment and the angle of attack increase, then galloping occurs at the certain combination of Reynolds number and angle of attack. After entering the critical Reynolds number range, vibrations with unsteady large amplitude occur as shown in Fig. 10 (a). The vibrations start diverging after a small step increase in wind speed as shown in Fig. 10 (b), and finally becomes a relative steady amplitude of vibration shown in Fig. 10 (c) at higher wind speed. When wind speed keeps increasing, at the certain value, the vibrations diminish as shown in Fig. 10 (d). The whole process of these vibrations is associated with the combination effect of Reynolds number and the angle of attack. It should be highlighted that the diverging process in Fig. 10 (b) and diminishing process in Fig. 10 (d) are not stable states, but they illustrate the development of the galloping. The unsteady amplitude vibration in Fig. 10 (a) is an 80s record and it keeps vibrating like this for at least 5 minutes during our observation. Another clear trait is that the horizontal displacement experiences several jumps in 80 seconds when a steady vertical vibration occurs in Fig. 10 (c). Although these jumps seem like a horizontal vibration, they do not have dominant frequency and are not periodic. This might be produced by the sudden change of drag coefficients in critical Reynolds number range where the small variation of the angle of attack can significantly influence flow pattern around the cylinder. Considering facts that the horizontal motion is much smaller than vertical and it does not show periodic characteristic, the vibration observed in this study can be treated as a vertical dominated galloping. On the other hand, this system is unlikely to have a coupled translational galloping theoretically because the natural frequency in the vertical 2.03Hz is approximate 24% higher than the value in the horizontal 1.64Hz (Nikitas and Macdonald, 2014). So the vertical response will be focused in discussing galloping response in next section, and the cross-wind galloping criterion will be used to estimate the galloping instability of this system.

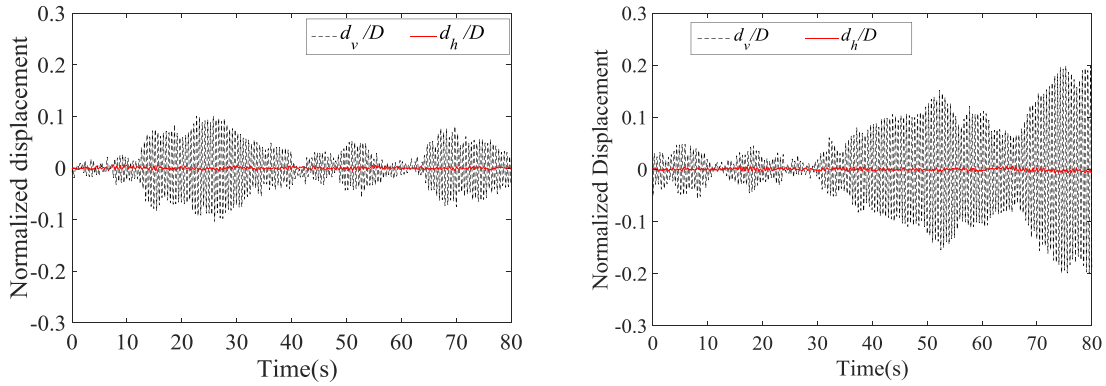

(a) α=26.94°, Re=1.61×10^5 (b) α=26.97°, Re=1.63×10^5

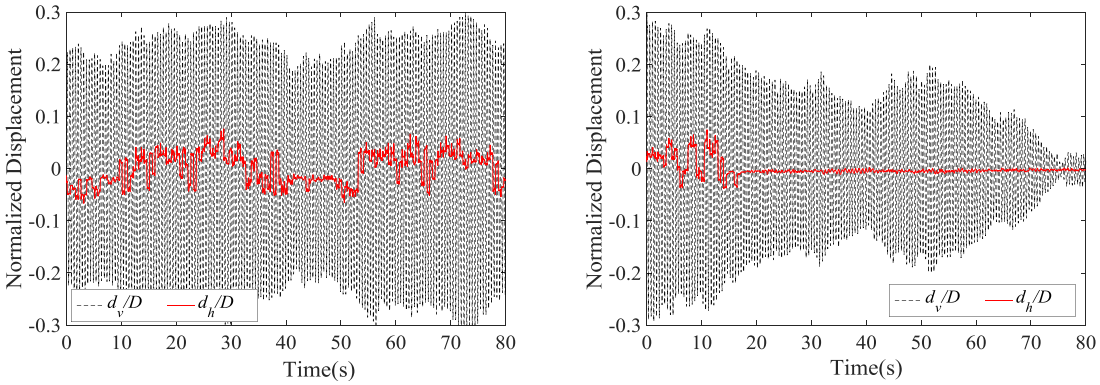

(c) α=26.93°, Re=1.69×10^5 (d) α=27.07°, Re=1.76×10^5

Fig. 10 Vibration at α_0=25.5° in different phases (a) α=26.94°, Re=1.61×10^5, (b) α=26.97°, Re=1.63×10^5, (c) α=26.93°, Re=1.69×10^5 and (d) α=27.07°, Re=1.76×10^5

4.2 Galloping Response

In order to illustrate the amplitudes of galloping responses in the vertical direction, the amplitudes of approximate 160 cycles were extracted from each displacement time history record. The amplitude is defined as half the peak to peak amplitude in each cycle. The normalized mean value of these 160 amplitudes (termed Amplitude/D) is shown in Fig. 11. The dash line shows the range of observed galloping approximate in Re=1.5×10^5-1.8×10^5 and α=26.5°-27.5°.

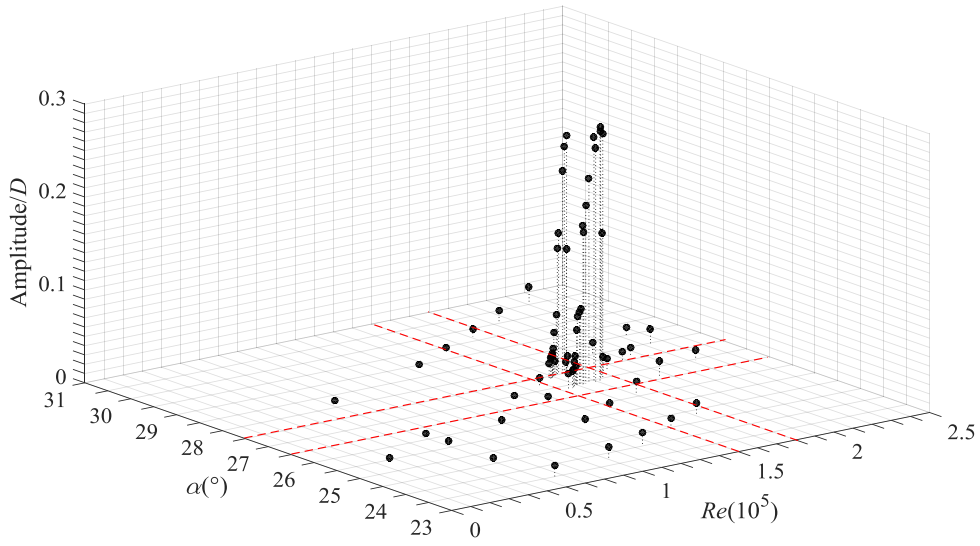

Fig. 11 Observed galloping and its normalized mean amplitude

Taking the case of α_0=25.5° as an example to show the variation of the galloping response amplitude with Reynolds number and angle of attack, The statistics of 160 amplitudes from each record are shown in Fig. 12, and the mean angle of attack is shown as well to illustrate the orientation of the cylinder. The line of the angle of attack in Fig. 12 is labeled by the right Y axes. By combining the angle of attack and Reynolds number labeled by X axes, the orientation and wind speed can be recognized. We define the vibration whose maximum amplitude is larger than 0.1D as galloping and a vibration whose coefficient of variation of amplitude is less than or around 10% as a steady galloping record like Fig. 10 (c) for an easy description. In term of this definition, galloping occurs in a range of at α=26.90°-27.08° and Re=1.59×10^5-1.76×10^5 and steady galloping occurs in a range of Re=1.66×10^5-1.74×10^5. The variation in the angle of attack shows a clear drop in the range of galloping. the drop means the aerodynamic moment is experiencing a relative decrease in magnitude and implies that galloping occurs at critical Reynolds numbers. Generally, the reduced velocity U/f_vD shown in top X axis in Fig. 12 is a significant parameter to identify whether the large vibration is the

quasi-steady process. In this study, the large vibrations occur at reduced velocity range from 34.6 to 38.9 which is not high enough to confirm that the quasi-steady theory should work in this case.

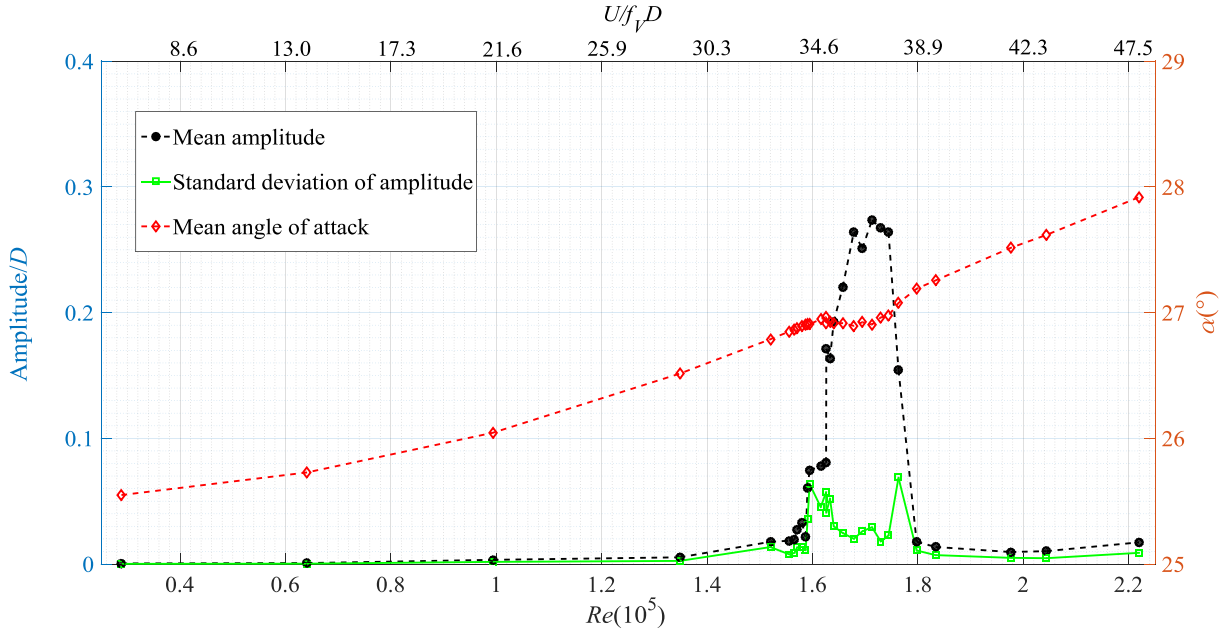

Fig. 12 Variation in galloping response amplitude with Reynolds number in dynamic tests with α_0=25.5°

5. Assessment of quasi-steady predication

Based on the quasi-steady assumption, mean aerodynamic coefficients obtained from the static tests and the structural parameters obtained from the free vibration tests can be used to estimate the galloping instability of structure by calculating the total damping. For wind induced vibrations, the total damping ratio ξ is the sum of the structural damping ratio and the aerodynamic damping ratio ξ_a. A diverge vibration occurs only if the total damping is negative. However, structural damping is positive, so this requires a negative aerodynamic damping. Based on the quasi-steady theory, the aerodynamic damping ratio of single-degree-of-freedom can be determined by the classic cross-wind criterion, as proposed by Den Hartog, which is used in most circumstances. In this study, the drag and lift coefficients is a function of the angle of attack and Reynolds number.

$$\xi_a = \frac{\rho D L U}{4 m \omega_V}\left(C_D + \frac{\partial C_L}{\partial \alpha}\right) \tag{4}$$

By using the weighted average aerodynamic force coefficients and the vertical natural frequency, $\omega_V = 2\pi f_v$, the aerodynamic damping ratio ξ_a is calculated through Eq.(4), and galloping instability is predicted using the total damping ratio.

Fig. 13 shows the observed galloping and the assessment of the quasi-steady prediction. For convenience comparing, the zero aerodynamic damping in dash line, the total damping ratio in grayscale and the observed vibration classified in three levels based on its mean amplitude are shown. As we expected, the negative aerodynamic damping estimated by Den Hartog's criterion appears at a certain range in which the reattachment makes a deep decrease of the curve of lift coefficients against the angle of attack. Furthermore, a steeper slope makes a stronger negative aerodynamic damping which may induce an easier occurrence of galloping. The region in which galloping is predicted is smaller than the region for negative aerodynamic damping because of the beneficial effect of positive structural damping. When the Reynolds number increases, the galloping is more likely happen at a larger angle of attack according to the predictions. This is caused by a fact of reattachment occurs at higher Reynolds number for a larger angle of attack.

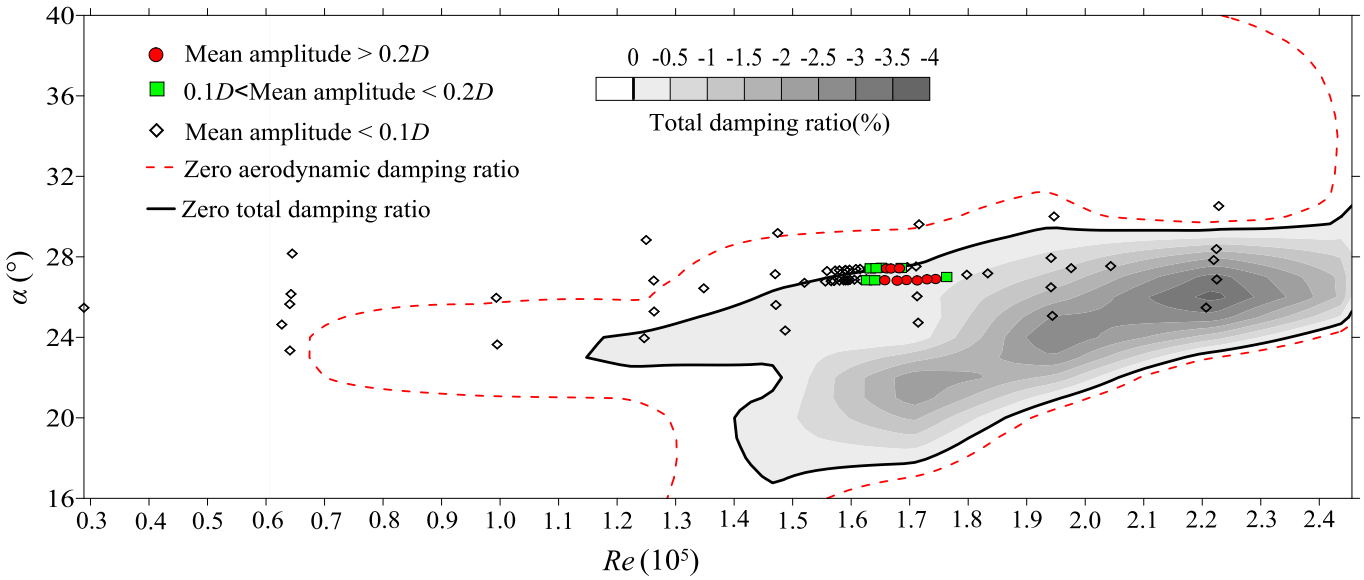

Fig. 13 Comparison of predicted galloping and observed galloping

Unfortunately, the occurrence of galloping in the dynamic tests does not agree well with the quasi-steady prediction. Even most cases of observed galloping are in the estimated galloping instability area, many cases in which galloping is predicted to occur from the theory did not exhibit large vibration in the dynamic tests. It is also hard to explain an unsteady amplitude galloping in term of the conventional galloping criterion. Taking all the observations into account, it seems the large vibrations are associated with the Reynolds number effect, but they cannot be explained by the conventional cross-wind galloping criterion in this instance.

The failure on predicting galloping in critical Reynolds number range by using quasi-steady assumption may relate to a flow sensitivity in this specific range. A fundamental principle of the conventional galloping criterion is that an interaction between a moving cylinder and the flow around it is weak enough to be simplified only with consideration of change mean aerodynamic force with velocity of cylinder, so the aerodynamic force on a moving cylinder is similar to the force on a static cylinder, and then the static force can be used to predict the galloping instability by the criterion. In the critical Reynolds number range, the flow around the cylinder is very sensitive to a small disturbance like surface roughness, turbulence intensity, and Reynolds number, and when the cylinder moves, even a small slow motion can pose a significant impact on flow and pressure distribution, so the dynamic characteristic of flow around the moving cylinder cannot be neglected anymore.

Other recent researches also show that unsteady flow or fluctuating aerodynamic forces in the critical Reynolds number range have a significant influence on vibration and should be considered. Benidir et al point out that aerodynamic force is unstable and sensitive to small circularity-defect in critical Reynolds number(Benidir et al, 2015). Matteoni and Ceorgakis reported a galloping of rough or distorted bridge cable in dry condition (Matteoni and Georgakis, 2015). In their study, the large vibration is observed in the critical Reynolds number range either under positive or negative aerodynamic damping. Matsumoto et al argue the unsteady galloping appears which response amplitude varies due to the fluctuations of Karman vortex intensity (Matsumoto et al, 2010). Nikitas and Macdonald believe that inherent flow pattern unsteadiness in the critical Reynolds number might be a reason for dry galloping (Nikitas and Macdonald, 2015). The common of these studies is a belief of dynamic characteristic of flow in critical Reynolds number is a reason of this large vibration like dry galloping. This also implies that only considering the mean aerodynamic force as the quasi-steady assumption does is not enough to explain the galloping in critical Reynolds number.

6. Conclusion

In conclusion, basing on a static and a dynamic wind tunnel tests, the static aerodynamic forces and galloping response are obtained. The static aerodynamic shows that a reattachment occurs on the elliptical cylinder in the critical Reynolds

number range for many angles of attack. It lowers drag coefficients, increases lift coefficients and induces a slope on the curve of lift coefficient against the angle of attack which may satisfy the conventional galloping criterion. Unsteady and steady amplitude galloping are observed in dynamic tests at reduced velocity from 34.6 to 38.9, Reynolds number from $1.5\times10^5$to 1.8×10^5 and angle of attack from 26.5° to 27.5°. All records show they are vertical dominated vibration and happen at a certain range of angle of attack in the critical Reynolds number range. Even the most observed galloping are in predicted instable range, numbers of tests supposing to have galloping in term of the prediction do not have large vibrations at all. This implies the quasi-steady assumption does not work well on estimating an occurrence of the galloping in the critical Reynolds number range at least in present tests with the reduced velocity below 40. The reason may related to the unsteadiness and sensitivity of flow at the critical Reynolds number which makes a strong interaction between a moving cylinder and flows around it.

Acknowledgements

The authors gratefully acknowledge the support of the National Natural Science Foundation of China (Grant Nos. 51378323) and China Scholarship Council.

References

Acampora, A., Macdonald, J.H.G., Georgakis, C.T., Nikitas, N., 2014. Identification of aeroelastic forces and static drag coefficients of a twin cable bridge stay from full-scale ambient vibration measurements. Journal of wind engineering and industrial aerodynamic 124, 90-98.

Benidir, A., Flamand, O., Gaillet, L., Dimitriadis, G., 2015. Impact of roughness and circularity-defect on bridge cables stability. Journal of Wind Engineering and Industrial Aerodynamics 137, 1-13.

Cao, S., Tamura, Y., 2008. Flow around a circular cylinder in linear shear flows at subcritical Reynolds number. Journal of Wind Engineering and Industrial Aerodynamics 96, 1961-1973.

Cheng, S., Larose, G.L., Savage, M.G., Tanaka, H., Irwin, P.A., 2008. Experimental study on the wind-induced vibration of a dry inclined cable--Part I: Phenomena. Journal of Wind Engineering and Industrial Aerodynamics 96, 2231-2253.

DenHartog, J.P., 1932. Transmission line vibration due to sleet. AIEE Transaction 51, 1074-1086.

Jakobsen, J.B., Andersen, T.L., Macdonald, J.H.G., Nikitas, N., Larose, G.L., Savage, M.G., McAuliffe, B.R., 2012. Wind-induced response and excitation characteristics of an inclined cable model in the critical Reynolds number range. Journal of Wind Engineering and Industrial Aerodynamics 110, 100-112.

Ma, W.Y., Liu, Q.K., Du, X.Q., Wei, Y.Y., 2015. Effect of the Reynolds number on the aerodynamic forces and galloping instability of a cylinder with semi-elliptical cross sections. Journal of Wind Engineering and Industrial Aerodynamics 146, 71-80.

Macdonald, J.H.G., Griffiths, P.J., Curry, B.P., 2008. Galloping analysis of stranded electricity conductors in skew winds. Wind and Structures, An International Journal 11, 303-321.

Macdonald, J.H.G., Larose, G.L., 2006. A unified approach to aerodynamic damping and darg/lift instabilities, and its application to dry inclined cable galloping. J Fluid Struct 22, 229-252.

Macdonald, J.H.G., Larose, G.L., 2008a. Two-degree-of-freedom inclined cable galloping--Part 1: General formulation and solution for perfectly tuned system. Journal of Wind Engineering and Industrial Aerodynamics 96, 291-307.

Macdonald, J.H.G., Larose, G.L., 2008b. Two-degree-of-freedom inclined cable galloping--Part 2: Analysis and prevention for arbitrary frequency ratio. Journal of Wind Engineering and Industrial Aerodynamics 96, 308-326.

Matsumoto, M., Yagi, T., Goto, M., Sakai, S., 2003. Rain–wind-induced vibration of inclined cables at limited high reduced wind velocity region. Journal of Wind Engineering and Industrial Aerodynamics 91, 1-12.

Matsumoto, M., Yagi, T., Hatsuda, H., Shima, T., Tanaka, M., Naito, H., 2010. Dry galloping characteristics and its mechanism of inclined/yawed cables. Journal of Wind Engineering and Industrial Aerodynamics 98, 317-327.

Matteoni, G., Georgakis, C.T., 2015. Effects of surface roughness and cross-sectional distortion on the wind-induced response

of bridge cables in dry conditions. Journal of Wind Engineering and Industrial Aerodynamics 136, 89-100.
Ng, Y.T., Luo, S.C., Chew, Y.T., 2005. On using high-order polynomial curve fits in the quasi-steady theory for square-cylinder galloping. J Fluid Struct 20, 141-146.
Nikitas, N., Macdonald, J.H.G., 2014. Misconceptions and generalisations of the Den Hartog Galloping criterion. Journal of Engineering Mechanics 140, 1-11.
Nikitas, N., Macdonald, J.H.G., 2015. Aerodynamic Forcing Characteristics of Dry Cable Galloping at Critical Reynolds Number. European Journal of Mechanics - B/Fluids 49, 243-249.
Nikitas, N., Macdonald, J.H.G., Jakobsen, J.B., Andersen, T.L., 2012. Critical Reynolds number and galloping instabilities: experiments on circular cylinders. Exp Fluids 52, 1295-1306.
Pa¨ıdoussis, M.P., Price, S.J., Langre, E.d., 2011. Fluid-Structure Interactions Cross-Flow-Induced Instabilities. Cambridge University Press, 32 Avenue of the Americas, New York, NY 10013-2473, USA.
Raeesi, A., Cheng, S., Ting, D.S.K., 2013. Aerodynamic damping of an inclined circular cylinder in unsteady flow and its application to the prediction of dry inclined cable galloping. Journal of Wind Engineering and Industrial Aerodynamics 113, 12-28.
Rodríguez, I., Lehmkuhl, O., Borrell, R., Paniagua, L., Pérez-Segarra, C.D., 2013. High Performance Computing of the Flow Past a Circular Cylinder at Critical and Supercritical Reynolds Numbers. Procedia Engineering 61, 166-172.
Schewe, G., 1986. Sensitivity of transition phenomena to small perturbations in flow round a circular cylinder. J Fluid Mech 172, 33-46.
Yagi, T., Naito, H., Liang, Z., Shirato, H., 2009. Evaluation of aerodynamic forces on inclined cable in consideration of end conditions of model for wind tunnel tests, Proceedings of the Eighth International Symposium on Cable Dynamics, Paris, France, pp. 151-158.
Zdravkovich, M.M., 1997. Flow Around Circular Cylinder. Oxford University Press, New York.